Acta Crystallographica Section B
Structural Science
ISSN 0108-7681

Local structural properties of $(Mn,Fe)Nb_2O_6$ from Mössbauer and X-ray absorption spectroscopy

Serena C. Tarantino,[a]* Paolo Ghigna,[b] Catherine McCammon,[c] Roberta Amantea[b] and Michael A. Carpenter[d]

[a]Dipartimento di Scienze della Terra, Università di Pavia, I-27100 Pavia, Italy, [b]Dipartimento di Chimica Fisica, Università di Pavia, I-27100 Pavia, Italy, [c]Bayerisches Geoinstitut, Universität Bayreuth, D-95440 Bayreuth, Germany, and [d]Department of Earth Sciences, University of Cambridge, Downing Street, Cambridge CB2 3EQ, England

Correspondence e-mail: tarantino@crystal.unipv.it

Received 26 November 2004
Accepted 14 March 2005

The $MnNb_2O_6$–$FeNb_2O_6$ solid solution has been investigated by Fe–K- and Mn–K-edge X-ray absorption (XANES and EXAFS), and Mössbauer spectroscopy. The first-shell $M-O$ bond lengths deduced from EXAFS show a fairly small compositional dependence. A degree of static disorder, which increases with increasing manganese content, is clearly seen by the loss of correlation for the next-neighbour (NN) interaction. Hyperfine parameters from Mössbauer spectra are consistent with variations in the average environment, as recorded by X-ray data. Line broadening of the Mössbauer spectra provides evidence for next-neighbour effects and is consistent with there being no significant clustering of Fe or Mn within the samples. There appear to be differences in the way the columbite structure accommodates Fe^{2+} and Mn^{2+} ions. In ferrocolumbite all the Fe octahedra are close to being identical, while there are local structural heterogeneities at a longer length scale, presumably in ordering the precise topology of polyhedra immediately adjacent to the octahedron. By contrast, the manganocolumbite seems to have some diversity in the precise coordination at the MnO_6 octahedra, but a greater uniformity in how the adjacent polyhedra are configured around them.

1. Introduction

The mixed occupancy of a site by differently sized ions, as in a solid solution, is often accompanied by local distortions that are absent (or anyway different) in the pure end-member compounds. The resultant strain fields may be isolated in the dilute limit, when a unit-cell scale strain will decay in magnitude as it extends away from the point where the structural change has occurred. At intermediate compositions the strain fractions will overlap, creating a net strain at a much longer scale length such as may be detected in the average lattice parameters. The local atomistic structural properties of a solid solution can often be measured only with difficulty, and it is not a simple matter to relate them to the macroscopic physical properties that represent an integration of all local states. Two limiting approaches have been used to interpret structural relaxation in solid solution. On the one hand, it is assumed that the bond lengths of one site, as determined by diffraction methods, vary monotonically as a function of composition across a binary solid solution. Hence, the mixed lattice is thought of as consisting of average (or virtual) sites. This has been described as the virtual crystal approximation (Martins & Zunger, 1984; Urusov, 2001), VCA. On the other hand, it is generally accepted that atomic radii remain approximately constant from structure to structure. Thus, the element-specific bonds largely retain the length and character in the

solid solution that they have in their respective end-members (Pauling model behaviour).

Spectroscopic methods provide the best tool to obtain direct and quantitative information on the local structure. In particular, ^{57}Fe Mössbauer spectroscopy gives information only on Fe—O bonding through measurements of the hyperfine parameters. EXAFS spectroscopy allows a direct characterization of the local structure around a chosen element, delivering bond distances and information about coordinating atoms and local distortions (for an introduction to EXAFS spectroscopy see, for example, Teo, 1986).

A Mössbauer and X-ray absorption spectroscopic study of columbite samples belonging to $FeNb_2O_6$–$MnNb_2O_6$ is presented in this paper. These oxide minerals exhibit electric and magnetic properties (antiferromagnets) that make them useful in many electronic devices. In particular, these compounds were found to have excellent dielectric properties at microwave frequencies (Maeda *et al.*, 1987; Lee, Kim & Hong, 1997; Lee, Hong & Kim, 1997; Pullar *et al.*, 2002; Zhang *et al.*, 2003, 2004, and references therein). Their high dielectric constants together with low dielectric losses attracted the interest of the telecommunication industry for their application as dielectric resonators and filters (Dong-Wan *et al.*, 2000). The average structure of the $FeNb_2O_6$–$MnNb_2O_6$ solid solution has been widely characterized (Weitzel, 1976; Wise *et al.*, 1985; Tarantino & Zema, 2005) by X-ray and neutron diffraction. These studies have shown that the columbite structure (depicted in Fig. 1) uniformly accommodates the replacement of Fe^{2+} ($^{[VI]}r$ = 0.78 Å) for Mn^{2+} ($^{[VI]}r$ = 0.84 Å; Shannon, 1976) and that all the geometrical parameters vary linearly (following Vegard's rule) as a function of Fe content. Evidence of the presence of local structural heterogeneities associated with Fe–Mn exchange is given by recent IR spectroscopic studies (Tarantino *et al.*, 2005). These small heterogeneities appear to extend to a few Å around the *A* site. In the present study spectroscopic investigations of the $FeNb_2O_6$–$MnNb_2O_6$ system provide information on the local structure around the *A* site at a shorter length than this.

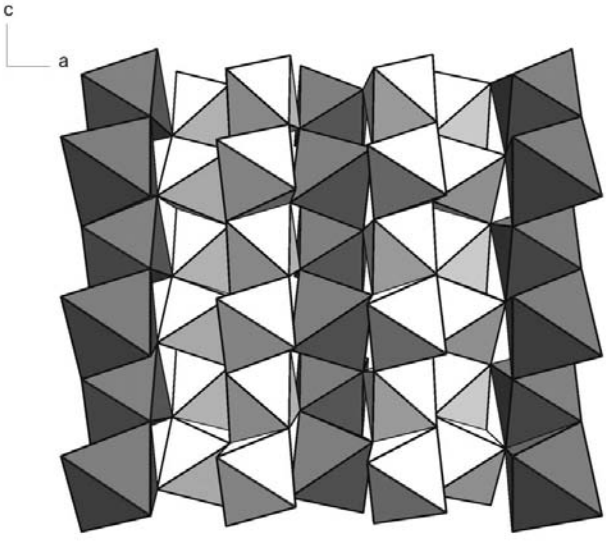

Figure 1
Perspective view of columbite structure (space group *Pbcn*; ranges of unit-cell dimensions for x = 0–1: $a \simeq$ 14.44–14.27, $b \simeq$ 5.77–5.73, $c \simeq$ 5.08–5.05 Å) showing the interconnection between the octahedral sites which form edge-sharing chains, cross-linked by shared corners.

2. Experimental

$Mn_{1-x}Fe_xNb_2O_6$ (x = 0, 0.05, 0.25, 0.50, 0.75, 1) samples were synthesized by solid-state reaction starting from stoichiometric amounts of Nb_2O_5, MnO, Fe and Fe_2O_3 of high purity (Aldrich > 99.9%). Pellets were prepared from the thoroughly mixed powders and allowed to react at 1223 K for a total time of at least 3 weeks in evacuated silica vials. X-ray powder diffraction (XRPD) and electron microprobe analysis (EMPA) inspections were performed to check the phase purity and homogeneity of the products.

The presence of a strong absorber such as Nb reduces the signal-to-noise ratio in Mössbauer spectra. Samples of intermediate composition (x = 0.05, 0.25, 0.50) which were used for the Mössbauer spectroscopy were therefore enriched with ^{57}Fe in order to obtain t_a = 2 (5 mg unenriched Fe per cm^2) following Long *et al.* (1983). Mössbauer spectra were recorded at room temperature in transmission mode on a constant acceleration Mössbauer spectrometer using a nominal 1.85 GBq ^{57}Co source in a 6 mm Rh matrix. The velocity scale was calibrated relative to metallic iron using the position certified for the standard reference material No.1541 of the former National Bureau of Standards; line widths of 0.28 mm s^{-1} for the outer lines of α-Fe were obtained at room temperature. The commercially available fitting program *NORMOS*90 (Brand, 1994) was used to fit the spectra.

The Fe–K- and Mn–K-edge X-ray absorption spectra were collected in transmission mode at liquid nitrogen temperature at the GILDA CRG beamline of the ESRF synchrotron radiation laboratory (Grenoble, France, experiment 08 01 625) using ion chambers as detectors and an Si(311) double-crystal monochromator.

The samples were mixed with polyethylene in an agate mortar and pressed into pellets for all the measurements. The amount of sample in the pellets was adjusted to ensure an edge jump of *ca* 1 logarithmic unit. Fe^{II} and Fe^{III} oxides were used as reference samples. EXAFS signal extraction from the raw spectra was performed using the *GNXAS* code (Filipponi *et al.*, 1995*a*,*b*). The *EXCURV*98 code (Binsted *et al.*, 1998) was used to analyze the Fourier-filtered EXAFS data in the range 1.5–4.2 Å. Amplitudes and phase shifts were calculated using the programs already mentioned. Distances were assumed to follow Gaussian distributions and therefore only the Gaussian part of the Debye–Waller factor (σ^2) was modelled.

3. Results

Mössbauer spectroscopy has been widely used in the past to evaluate the degree of cation order (Wenger *et al.*, 1991; Augsburger *et al.*, 1999; dos Santos *et al.*, 1999, 2001; Sosa *et al.*, 2002) as well as magnetic interaction (Zawislak *et al.*, 1995) and crystal field effects (Eibschütz *et al.*, 1967) in columbite

and tantalite oxides. In completely ordered (Mn,Fe)Nb_2O_6 columbite Fe is restricted to the *A* site. Mössbauer spectra, shown in Fig. 2, are all characterized by the presence of a single doublet, the hyperfine parameters of which correspond to Fe^{II} in octahedral coordination. The use of ^{57}Fe enables high signal-to-noise ratios to be obtained in spite of the presence of Nb, but also introduces thickness effects. We therefore fitted the spectra using the full transmission integral to account for these effects. The dimensionless effective thickness of each sample was calculated from sample geometry and chemical composition.

Hyperfine parameters derived from the Mössbauer spectra can be used to characterize the local electronic environment about Fe atoms. The hyperfine parameters for (Mn,Fe)Nb_2O_6 columbite (Fig. 3) are similar to those already reported in the literature (Wenger *et al.*, 1991; Zawislak *et al.*, 1995; dos Santos *et al.*, 2001) for the *A* site. The variation of the centre shift and

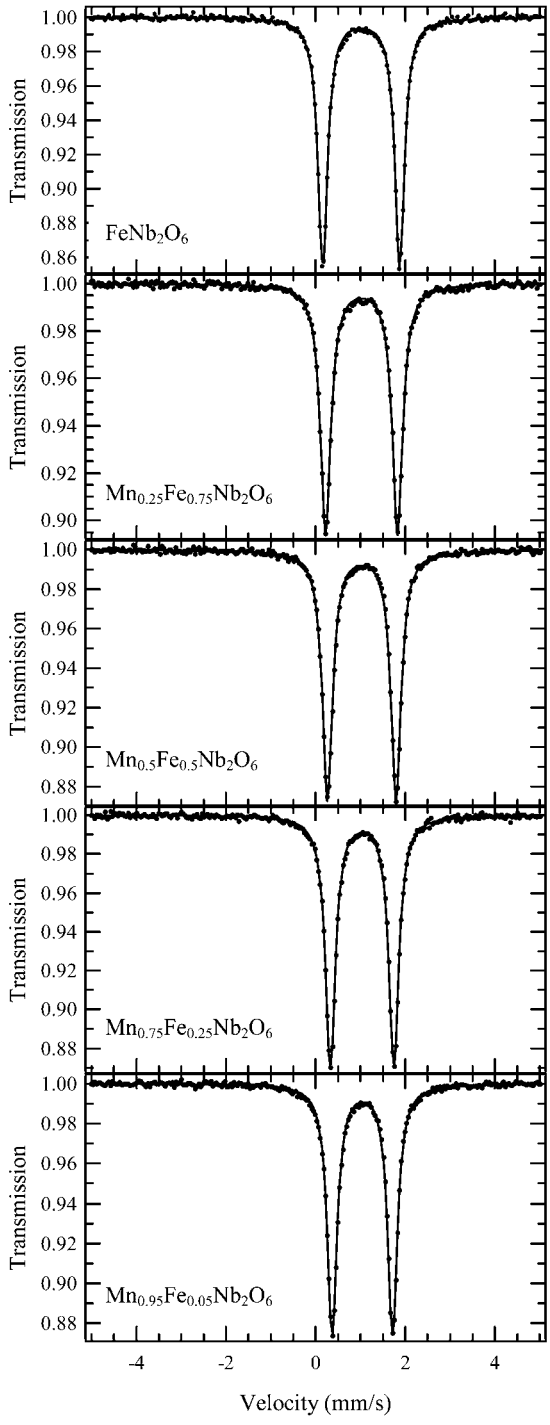

Figure 2
Room-temperature Mössbauer spectra of $Mn_{1-x}Fe_xNb_2O_6$ columbite samples. The spectra were fitted using the full transmission integral and show one doublet corresponding to Fe^{2+} in an octahedral coordination.

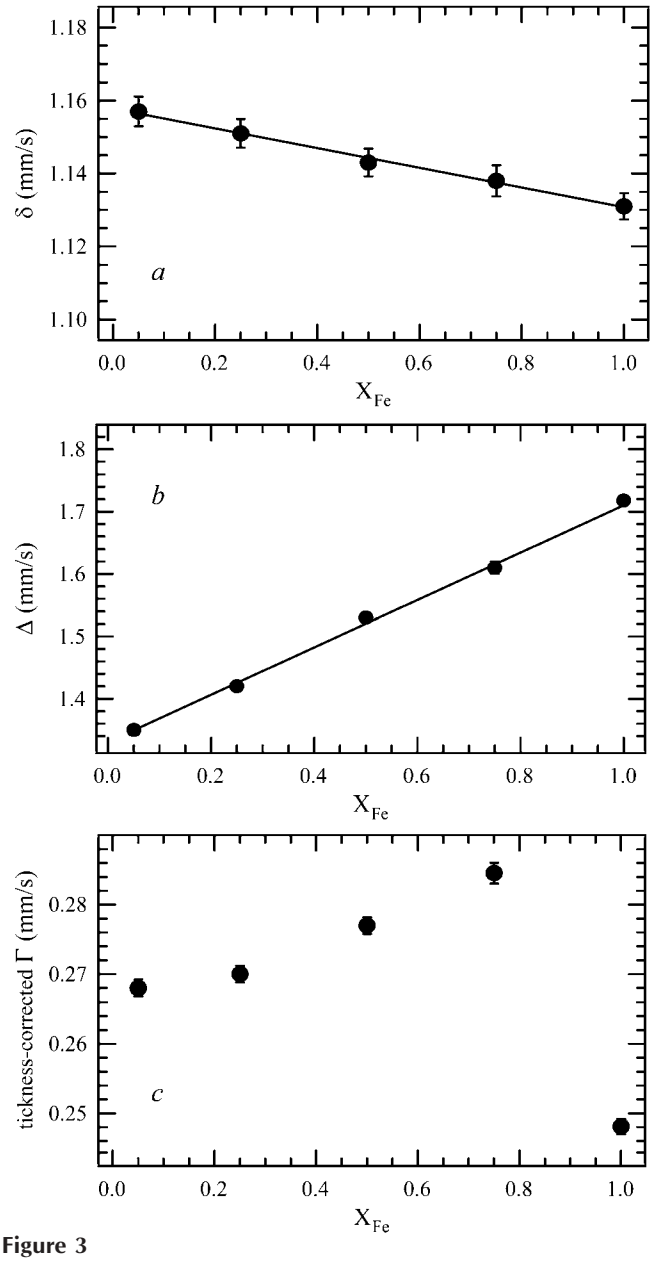

Figure 3
Variation of the Mössbauer hyperfine parameters for the *A* site as a function of composition across the $Mn_{1-x}Fe_xNb_2O_6$ system: (*a*) isomer shift; (*b*) quadrupole splitting; (*c*) total line widths; line widths have been corrected for absorber thickness effects. The line width for the absorber thickness $t_a = 2$ has been calculated according to Margulies & Ehrmann (1961).

the quadrupole splitting of the absorption doublets with Fe/Mn content provides information about changes in the average Fe environment. The variation of the isomer shift of the analysed samples as a function of composition is shown in Fig. 3(*a*); a linear trend is apparent. The centre shift of the doublet consists of the isomer shift (IS) plus the second-order Doppler shift. As the latter is approximately equal for all the samples considered here, we will take the centre shift to be equivalent to the IS, which is, in turn, inversely proportional to the difference between the *s* electron density at the Fe nuclei in the source and those in the absorber. Therefore, the IS corresponding to Fe^{2+} on the *A* site of the columbite structure decreases with increasing Fe content. This is because the *s* electron density at the Fe nucleus is increased as a consequence of a 'contraction' in the Fe—O bond lengths with increasing ferrocolumbite content, as shown by Tarantino *et al.* (2005). The quadrupole splitting (QS) can be regarded as the sum of the terms related to contributions from the valence electrons and the rest of the crystal (Ingalls, 1964). When distortion from cubic symmetry is small the valence term dominates the QS and increasing distortion produces greater QS. When distortion from cubic symmetry is large the lattice term dominates the QS, which then increases with decreasing site distortion. Since the *A* octahedron in columbites is quite distorted, the increase in QS at the *A* site (Fig. 3*b*) with increasing Fe content may be due to a decrease in site distortion. In the case of two Fe sites in neptunite, $KNa_2Li(Fe,Mn,Mg)Ti_2Si_8O_{24}$, it has been shown (Kunz *et al.*, 1991) that the edge-length distortion (ELD) correlates inversely with quadrupole splitting. For columbite, ELD values for the *A* site obtained by refinement of X-ray data from the same suite of samples also decrease linearly with increasing Fe content (Tarantino & Zema, 2005).

While IS and quadrupole splitting give information on the average structure of the Mössbauer absorber, the width of the absorption peaks provides an indication of the differences and variations of the local chemical environment of Fe atoms within a single sample. In Fig. 3(*c*) the variation in the line width of Mössbauer doublets (thickness corrected) as a function of Fe content is shown. Apart from the Fe end-member showing sharper lines, a systematic trend with composition is evident. It is reasonable to assume that instrument-related broadening is the same for all the spectra reported and that differences in the line widths reflect the presence of local heterogeneities about the Fe atoms within samples. Effects such as compositional heterogeneity and microstructural domains change the relative proportions of the different local environments around the Fe atoms and therefore can all give rise to spectral line broadening. In our sample the compositional heterogeneity, as measured by electron microprobe, appeared to be insufficient to give rise to a significant contribution to line width. No evidence of microstructural domains was found. The broadening, or at least its variations with composition, may be due to the presence of slightly different next-nearest neighbour environments in the samples.

Fig. 4 shows the k^3 weighted Fe–K-absorption edge EXAFS for $FeNb_2O_6$, $Mn_{0.25}Fe_{0.75}Nb_2O_6$ and $Mn_{0.5}Fe_{0.5}Nb_2O_6$. In Fig. 5 the same data are shown for the Mn–K-edge EXAFS of $MnNb_2O_6$, $Mn_{0.25}Fe_{0.75}Nb_2O_6$ and $Mn_{0.5}Fe_{0.5}Nb_2O_6$. Unfortunately, due to the huge absorption of the samples, mainly caused by the Nb–L edges, it has been impossible to measure more diluted samples in absorption mode. The shorter *k* range

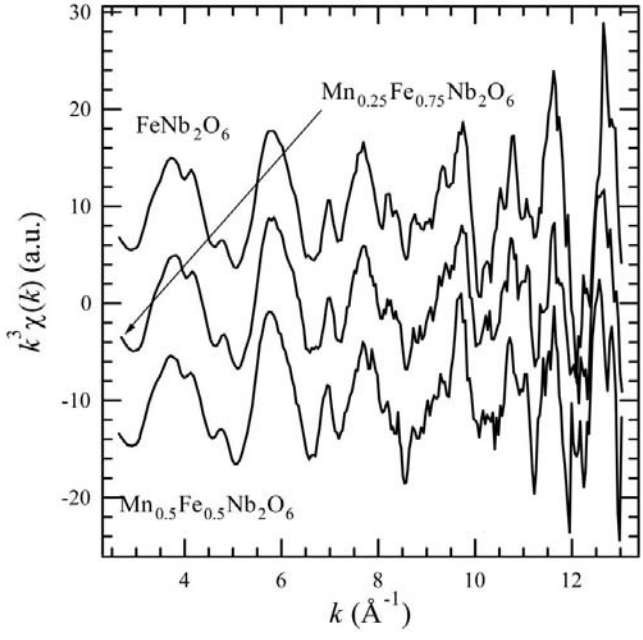

Figure 4
EXAFS signal at the Fe–K edge for $FeNb_2O_6$, $Mn_{0.25}Fe_{0.75}Nb_2O_6$ and $Mn_{0.5}Fe_{0.5}Nb_2O_6$ samples.

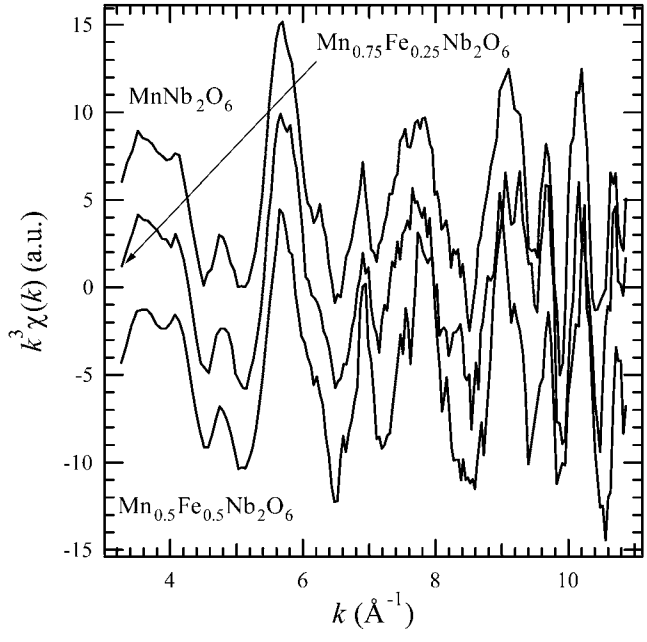

Figure 5
EXAFS signal at the Mn–K edge for $Mn_{0.5}Fe_{0.5}Nb_2O_6$, $Mn_{0.75}Fe_{0.25}Nb_2O_6$ and $MnNb_2O_6$ samples.

used for the Mn–K edge is due to the presence of the Fe–K edge. Fig. 6(*a*) shows the Fe–K-edge EXAFS signal, after Fourier filtering in the range 1.5–4.2 Å, for $FeNb_2O_6$. Fig. 6(*b*) shows the corresponding Fourier transform. In Fig. 7 the same data are shown for the Mn–K edge in $MnNb_2O_6$.

For both the Fe–K and Mn–K edges, in the Fourier transform the oxygen coordination shells give rise to an unresolved peak at *ca* 2 Å. For the Mn–K edge, the second peak at *ca* 3.5 Å is due to the Mn/Fe next-nearest neighbours; the smaller peak at *ca* 4 Å is mainly due to Nb atoms in the *B* site of the columbite structure. Regarding the Fe–K-edge spectra, the Fe/Mn next-nearest neighbours are responsible for the peak at *ca* 3.2 Å, while the peaks between 3.5 and 4.2 Å are mainly due to Nb atoms on the *B* site. The better resolution of these peaks, when compared with those of the Mn–K-edge spectra, is due to the wider *k* range available at the Fe–K edge.

As we are mainly concerned with comparisons between the local chemical environment of Mn and Fe in the $Mn_{1-x}Fe_xNb_2O_6$ solid solution, the following analysis will be focused on the parameters associated with the first two shells (next neighbours and next-nearest neighbours), which are also

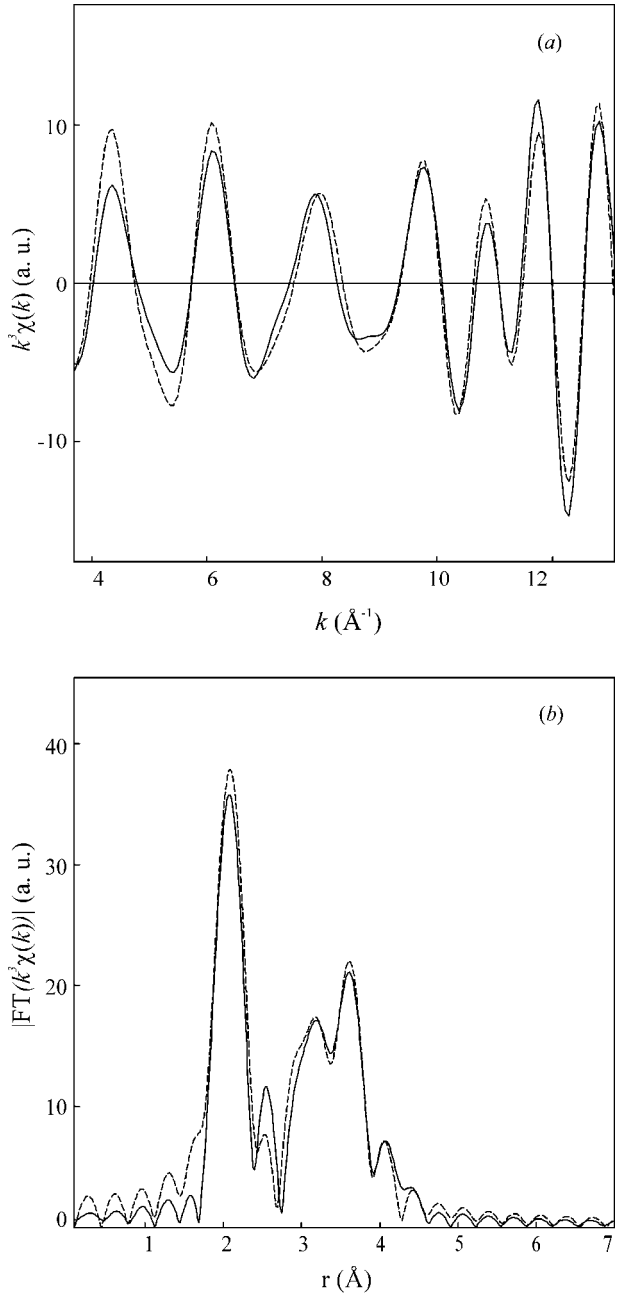

Figure 6
(*a*) Fe–K-edge EXAFS signal (dotted line) after Fourier filtering in the range 1.5–4.2 Å for $FeNb_2O_6$; (*b*) the corresponding Fourier transform (dotted line) is shown. The solid lines refer to the fit according to the model described in the text.

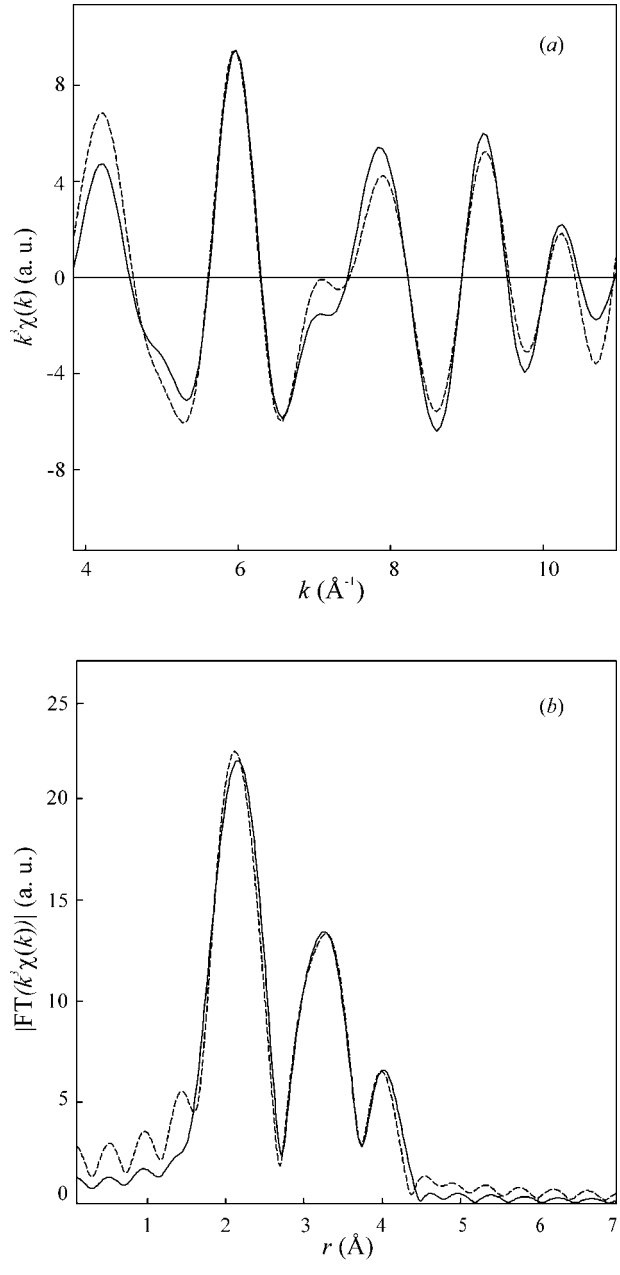

Figure 7
(*a*) Mn–K-edge EXAFS signal (dotted line) after Fourier filtering in the range 1.5–4.2 Å for $MnNb_2O_6$; (*b*) the corresponding Fourier transform (dotted line) is shown. The solid lines refers to the fit according to the model described in the text.

Table 1
Fit results and statistics.

X_{Fe}	$A-O$ (Å)	$A-A$ (Å)	$\sigma^2(A-O)$ (Å^2)	$\sigma^2(A-A)$ (Å^2)	No. of independent points	No. of fitted parameters	Experimental mean error bar	χ^2
Fe–K edge								
1	2.110 (8)	3.155 (6)	0.0042 (3)	0.0012 (4)	27	11	3×10^{-4}	5.17
0.75	2.123 (7)	3.164 (5)	0.0052 (3)	0.0034 (3)	27	11	2×10^{-4}	2.73
0.5	2.122 (6)	3.192 (6)	0.0052 (2)	0.005 (1)	27	11	2×10^{-4}	3.32
Mn–K edge								
0.5	2.158 (5)	3.275 (5)	0.0082 (3)	0.0007 (6)	24	13	4×10^{-4}	4.43
0.25	2.163 (4)	3.29 (2)	0.0061 (3)	0.0050 (5)	24	13	4×10^{-4}	4.32
0	2.18 (1)	3.29 (3)	0.0067 (3)	0.0047 (5)	24	13	5×10^{-4}	5.68

the most reliable and those that are affected by correlation to the slightest extent.

Fig. 8 displays the mean Fe—O and Mn—O distances derived from the EXAFS fittings as a function of the Fe content. The error bars in this and in the following figures have been calculated by the *EXCURV*98 code according to standard procedures (IXS Standards and Criteria Subcommittee Reports, 2000). The fit results are reported for each composition in Table 1. Within experimental error, the fitted distances show a slight dependence on X_{Fe}, whilst compositional dependence is a little more evident in the Mn—O distances. For comparison the $A-O$ mean distances, calculated from Rietveld refinements (Tarantino *et al.*, 2005), are shown in the same figure: they are in fact a compositional average of those derived by EXAFS. It is worth noting the excellent agreement between the EXAFS and Rietveld refinements for the $A-O$ distances of the end-members. Further confirmation of this behaviour can be obtained from Fig. 9, in which the $A-A$ distances are plotted as a function of Fe content. In this case, agreement between EXAFS and the Rietveld refinements is better, but the errors in the $A-A$ distance obtained by EXAFS increases with decreasing Fe content. Quite a similar result is obtained by looking at the σ^2 factors that are displayed in Figs. 10 and 11 for the $A-O$ and $A-A$ distances, respectively. For the $A-O$ distances, the σ^2 factors are almost constant, with a small decrease towards the pure $FeNb_2O_6$ composition. A considerable exception is the σ^2 factor for the Mn—O distance in $Mn_{0.5}Fe_{0.5}Nb_2O_6$, which has the greatest value. The same trend is also found for the σ^2 factors of the next-nearest neighbours shell, but, in this case, the σ^2 factor for the Mn—A distance in $Mn_{0.5}Fe_{0.5}Nb_2O_6$ has the smallest value. The error in the σ^2 parameter for the Fe—A distance decreases with increasing Fe content.

4. Discussion and conclusions

Spectroscopic results reveal a complex but systematic response of the columbite structure type to Mn–Fe substitution on the A octahedral site. The first-neighbour Fe—O bond lengths remain close to the distance in the pure end-member. Mn—O distances gained from EXAFS fitting decrease slightly with increasing X_{Fe}. The element-specific AO bonds show a different compositional dependence from the AO bond lengths determined by Rietveld refinement. Bond distances from X-ray refinement are in fact an average value of all Fe—O and Mn—O bond lengths over several unit cells. It is worth

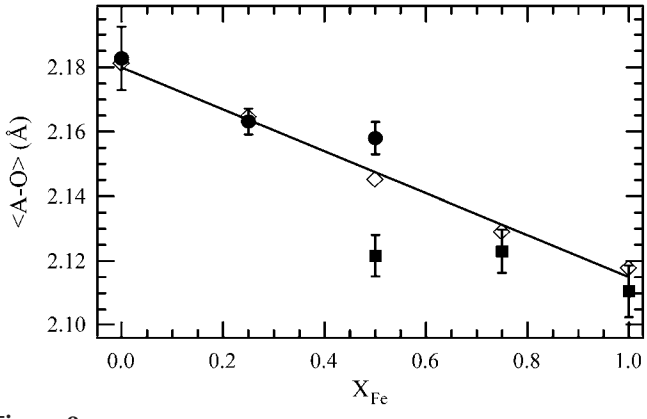

Figure 8
Variation of $A-O$ distances as a function of X_{Fe} across the $Mn_{1-x}Fe_xNb_2O_6$ system. Solid symbols: Mn—O and Fe—O mean distances from the EXAFS analysis; open diamonds: average $A-O$ distances from Rietveld refinement of X-ray data from the same suite of samples (Tarantino *et al.*, 2005).

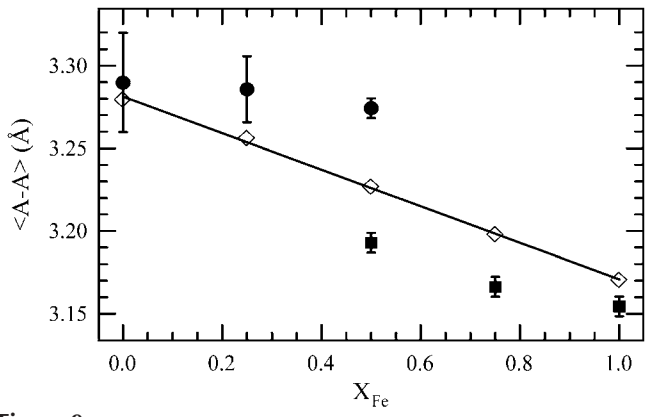

Figure 9
Variation of $A-A$ distances as a function of X_{Fe} across the $Mn_{1-x}Fe_xNb_2O_6$ system. Solid symbols: Mn—A and Fe—A mean distances from the EXAFS analysis; open diamonds: average $A-A$ from Rietveld refinement of X-ray data from the same suite of samples (Tarantino *et al.*, 2005).

noting, in this regard, the fairly good agreement between the *A*O distances from X-ray and EXAFS refinement in the two end-members.

The possibility that Fe would cluster to form Fe-rich domains has been discarded, as the small compositional dependence of the first shell Fe—O distance might also suggest. If such Fe-rich domains were present, not just the first shell distances, but also the distances to further shells should also be the same as in the end-members. Clearly this is not the case. Furthermore, the Lorentzian shape as well as the symmetry of the peaks of the Mössbauer spectra give no indication of such clustering. On the contrary, the observed peak-broadening can be indicative of a lack of short-range order within the sample, because a higher degree of short-range order (SRO) would lead to fewer Fe environments and sharper peaks. In addition, it is worth noting that the presence of Fe-rich domains would probably lead to a non-linear variation of IS as a function of composition.

The observed behaviour is fairly close to the so-called 'state of alternating bond', in which Fe—O and Mn—O bonds keep, to a rather large degree, the length and character they have in the respective end-members. The second-neighbour cation–cation distances also show a similar trend to that found for M^{2+}—O; they in fact form, as a function of composition, a roughly linear trend midway between the average (virtual crystal distance) and the end-member limit. The observed small differences in the actual Mn—O bond lengths within each sample at high Mn content give rise to a spread of the Mn—M^{2+} distances, evidenced by the increase of the fitting error with decreasing X_{Fe}. Such a spread of the Mn—M^{2+} distances along the chain is a consequence not only of actual Mn—O bond-length variations within the sample, but also of the different off-centre displacement of the Mn cations. Octahedral chains share semi-adjacent edges (hence the cations are brought into contact) and minimize the cation–cation repulsion along the octahedral chain by moving along the crystallographic *b* direction. The off-centre displacement is larger for Mn^{2+} cations than for Fe^{2+} because of their larger size.

In order to quantify the variations of the first-shell bond lengths across a substitutional solid solution, a relaxation parameter ε has been defined (Martins & Zunger, 1984). For *B* impurity substitution in $A_xB_{1-x}C$ solid solution, $\varepsilon = (R_{BC} - R^0_{AC})/(R^0_{BC} - R^0_{AC})$, where R_{BC} is the actual *B*—*C* distance and R^0_{BC} and R^0_{AC} are the *BC* and *AC* bond lengths in the pure end-members. The two limiting cases, discussed above, of the Virtual Crystal Approximation (Vegard's law) and Pauling's model have values of 0 and 1, respectively. Based on the observed EXAFS distances the relaxation parameter ε in the analysed columbite solid solution is *ca* 0.8 and *ca* 0.7 for Fe^{2+} and Mn^{2+}, respectively.

The topology of the bonding network plays an important role in determining the extent of the dependence of bond length on composition in solid solution, as suggested by Dollase (1980). EXAFS studies of alkali halide solid solutions show a significant variation with the composition of first-shell bond lengths, yielding relaxation parameters of 0.4–0.6 (Dollase, 1980; Boyce & Mikkelsen, 1985; Yokoyama *et al.*, 1990; Sato *et al.*, 1992; Frenkel *et al.*, 1996). On the other hand, a nearly complete composition independence of the Mn—O distances has been observed across the $MnCO_3$–$CaCO_3$ (Lee *et al.*, 2002) solid solution with a relaxation parameter of *ca* 0.9. The calcite structure consists of corner-sharing polyhedra and this allows it to respond to cation substitution on an octahedral site through bond bending with minor distortion of the adjacent octahedra. On the other hand, the rock salt structure is highly interconnected and less flexible so that the strain is accommodated over a greater radial distance. The columbite structure is built up of edge-sharing octahedra, but interpolyhedral connections can still compensate for mismatch between the volumes of sites, by varying the angles between two edge-sharing faces of adjacent polyhedra. Thus, distortion appears to be on a local length scale, intermediate between carbonate and alkali halide solid solutions, perhaps within individual unit cells.

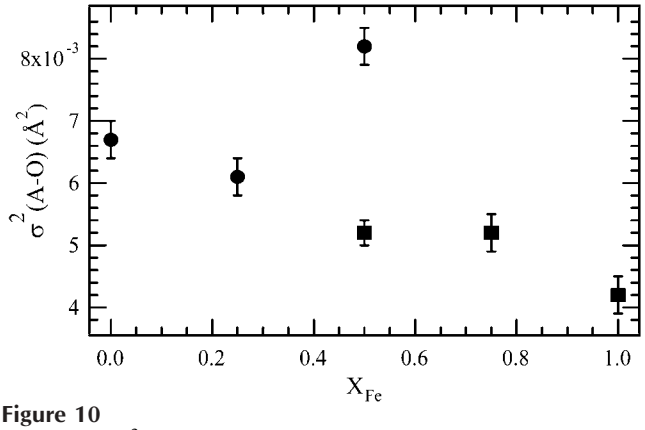

Figure 10
Variation of σ^2 factors of the *A*—O distance across the $Mn_{1-x}Fe_xNb_2O_6$ system as a function of the Fe content. Solid circles: Mn—O mean distances; solid squares: Fe—O mean distances.

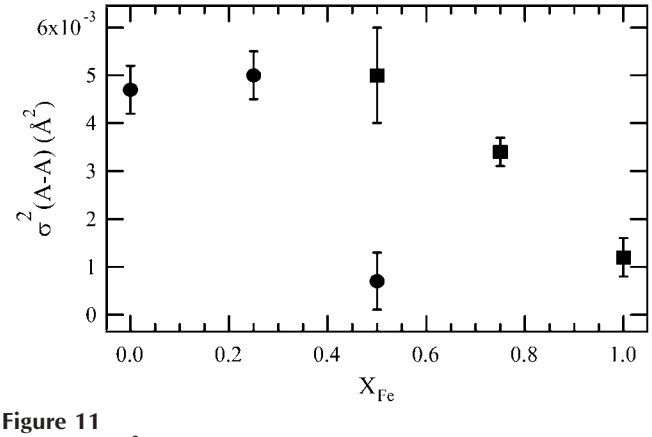

Figure 11
Variation of σ^2 factors of the *A*—*A* distance across the $Mn_{1-x}Fe_xNb_2O_6$ system as a function of the Fe content. Solid circles: Mn—*A* mean distances; solid squares: Fe—*A* mean distances.

It is evident that the Fe^{2+} atoms keep the same coordination polyhedron as in the end-member across the solid solution, although a slight increase of the distortion with increasing Mn content has been indicated by the decrease of QS. This is achieved by imposing a distortion on the immediate neighbour, as evidenced by powder IR study (Tarantino *et al.*, 2005). On the other hand, manganocolumbite seems to show some diversity in the precise coordination at the MnO_6 octahedra. This fact can be justified by the d^5 electronic configuration of Mn^{II}, which results in a null crystal field stabilization energy. With respect to ferrocolumbite, the Mn end-member shows a greater uniformity in configuration of the adjacent polyhedra. Strain fields associated with cation substitution across the solid solution are highly localized. The distortions appear to be fairly weak and fade away over a length scale of few unit cells.

G. Ciatto (ESRF-GILDA CRG) is gratefully acknowledged for considerable help during the EXAFS measurements and for helpful discussions. The authors also thank M. Zema for fruitful discussions. The manuscript benefited from the comments of two anonymous reviewers. This work has been partially supported by the Italian MIUR project 'Mineral physics and technological applications of columbite–tantalite–tapiolite system'. The Mössbauer experiments were performed at the Bayerisches Geoinstitut under the EU 'IHP – Access to Research Infrastructures' Program (Contract No. HPRI-1999-CT-00004 to D. C. Rubie).

References

Augsburger, M. S., Pedregosa, J. C., Sosa, G. M. & Mercader, R. C. (1999). *J. Solid State Chem.* **143**, 219–223.
Binsted, N., Gurman, S. J., Campbell, T. C. & Stephenson, P. C. (1998). *EXCURV*98. SERC Daresbury Laboratory, UK.
Boyce, J. B. & Mikkelsen, J. C. (1985). *Phys. Rev. B*, **31**, 6903–6905.
Brand, R. A. (1994). *NORMOS*90. Laboratorium für Angewandte Physik, Universität Duisburg, Germany.
Dollase, W. A. (1980). *Phys. Chem. Miner.* **6**, 295–304.
Dong-Wan, K., Deok-Yang, K. & Kug Sun, H. (2000). *J. Mater. Res.* **15**, 1331–1335.
Eibschütz, M., Ganiel, U. & Shtrikman, S. (1967). *Phys. Rev.* **156**, 259–261.
Filipponi, A., Di Cicco, A. & Natoli, C. R. (1995*a*). *Phys. Rev. B*, **52**, 15122–15134.
Filipponi, A., Di Cicco, A. & Natoli, C. R. (1995*b*). *Phys. Rev. B*, **52**, 15135–15149.
Frenkel, A. I., Stern, E. A., Voronel, A. & Heal, S. M. (1996). *Solid State Commun.* **99**, 67–71.
Ingalls, R. (1964). *Phys. Rev. A*, **133**, 787–795.
IXS Standards and Criteria Subcommittee Reports (2000). http://ixs.iit.edu/subcommittee_reports/sc/.
Kunz, M., Armbruster, T., Lager, G. A., Schultz, A. J., Goyette, R. J. & Lottermoser, W. (1991). *Phys. Chem. Miner.* **18**, 199–213.
Lee, H. J., Hong, K. S. & Kim, I. T. (1997). *Mater. Res. Bull.* **32**, 847–855.
Lee, H. J., Kim, I. T. & Hong, K. S. (1997). *Jpn. J. Appl. Phys.* **36**, 1318–1320.
Lee, Y. J., Reeder, R. J., Wenkus, R. W. & Elzinga, E. J. (2002). *Phys. Chem. Miner.* **29**, 585–594.
Long, G. L., Cranshaw, T. E. & Longworth, G. (1983). *Möss. Effect Ref. Data J.* **6**, 42–49.
Maeda, M., Yamamura, T. & Ikeda, T. (1987). *Jpn. J. Appl. Phys.* **26**, 76–79.
Margulies, S. & Ehrmann, J. R. (1961). *Nucl. Instrum. Methods*, **12**, 131–137.
Martins, J. L. & Zunger, A. (1984). *Phys. Rev. B*, **30**, 6217–6220.
Pullar, R. C., Breeze, J. D. & Alford, N. M. (2002). *Key Eng. Mater.* **224–226**, 1–4.
Santos, C. A. dos, Zawislak, L. I., Antonietti, V., Kinast, E. J. & da Cunha, J. B. M. (1999). *J. Phys. Cond. Matter*, **11**, 7021–7033.
Santos, C. A. dos, Zawislak, L. I., Kinast, E. J., Antonietti, V. & da Cunha, J. B. M. (2001). *Braz. J. Phys.* **31**, 616–631.
Sato, H., Yokoyama, T., Ono, I., Kameyuki, K. & Ohta, T. (1992). *Jpn. Appl. Phys.* **31**, 1118–1123.
Shannon, R. D. (1976). *Acta Cryst.* A**32**, 751–767.
Sosa, G. M., Augsburger, M. S. & Pedregosa, J. C. (2002). *Eur. J. Mineral.* **14**, 627–636.
Tarantino, S. C. & Zema, M. (2005). *Am Mineral.* In the press.
Tarantino, S. C., Zema, M., Maglia, F., Domeneghetti, M. C. & Carpenter, M. A. (2005). Submitted for publication.
Teo, B. K. (1986). *EXAFS: Basic Principles and Data Analysis.* Berlin: Springer.
Urusov, S. V. (2001). *Solid Solution in Silicate and Oxide Systems*, edited by C. A. Gaiger, EMU Notes Mineralogy 3, pp. 121–153. Budapest University Press.
Weitzel, H. (1976). *Z. Kristallogr.* **144**, 238–258.
Wenger, M., Ambruster, T. & Geiger, C. (1991). *Am. Mineral.* **76**, 1897–1904.
Wise, M. A., Turnock, A. C. & Černý, P. (1985). *Neues Jahrb. Miner. Monat.* **8**, 372–378.
Yokoyama, T., Takamatsu, F., Seki, K., Miyake, K., Tani, T. & Otha, T. (1990). *Jpn. J. Appl. Phys.* **29**, L1486–L1489.
Zawislak, L. I., da Chuna, J. B. M., Vasquez, A. & dos Santos, C. A. (1995). *Solid State Commun.* **94**, 345–348.
Zhang, Y. C., Yue, Z. X., Gui, Z. L. & Li, L. T. (2003). *Mater. Lett.* **57**, 4531–4534.
Zhang, Y. C., Wang, J., Yue, Z. X., Gui, Z. L. & Li, L. T. (2004). *Ceram. Int.* **30**, 87–91.